Orbital-Radar v1.0.0: A tool to transform suborbital radar observations to synthetic EarthCARE cloud radar data

Lukas Pfitzenmaier[1], Pavlos Kollias[1,2], Nils Risse[1], Imke Schirmacher[1], Bernat Puigdomenech Treserras[3], and Katia Lamer[4]

[1]Institute for Geophysics and Meteorology, University of Cologne, Cologne, Germany
[2]School of Marine and Atmospheric Sciences, Stony Brook University, Stony Brook, NY, USA
[3]Department of Atmospheric and Oceanic Sciences, McGill University, Montreal, Canada
[4]Environmental and Climate Sciences Department, Brookhaven National Laboratory, Upton, NY, USA

Correspondence: Lukas Pfitzenmaier (l.pfitzenmaier@uni-koeln.de)

Abstract. The Earth Cloud, Aerosol and Radiation Explorer (EarthCARE) satellite developed by the European Space Agency (ESA) and the Japan Aerospace Exploration Agency (JAXA) launched in May 2024 carries a novel 94-GHz Cloud Profiling Radar (CPR) with Doppler capability. This work describes the open-source instrument simulator Orbital-Radar, which transforms high-resolution radar data from field observations or forward simulations of numerical models to CPR primary measurements and uncertainties. The transformation accounts for sampling geometry and surface effects. We demonstrate Orbital-Radar's ability to provide realistic CPR views of typical cloud and precipitation scenes. The presented case studies show small-scale convection, marine stratus clouds and Arctic mixed-phase cloud cases. These results provide valuable insights into the capabilities and challenges of the EarthCARE CPR mission and its advantages over the CloudSat CPR. Finally, Orbital-Radar allows for ~~the evaluation of kilometer-scale~~ evaluating kilometre-scale numerical weather prediction models with EarthCARE CPR observations. So, Orbital-radar can generate Cal/Val data sets already pre-launch. Nevertheless, an evaluation of synthetic CPR output data to accurate EarthCARE CPR data is missing.

1 Introduction

Spaceborne radars offer a unique opportunity to monitor clouds and precipitation globally. For instance, the National Aeronautics and Space Administration (NASA) CloudSat Cloud Profiling Radar (CloudSat CPR; (Stephens et al., 2008, 2018)) enabled several advances in cloud and precipitation physics (Rapp et al., 2013; Stephens et al., 2018; Battaglia et al., 2020b). In 2024, the next generation CPR in space will launch onboard the Earth Cloud, Aerosol and Radiation Explorer (EarthCARE) satellite (Illingworth et al., 2015; Wehr et al., 2023). The EarthCARE CPR will be the first Doppler radar in space thus providing the first set of global Doppler velocity measurements (Kollias et al., 2022). In addition to the Doppler capability, the EarthCARE CPR will have higher sensitivity than its predecessor (-35 dBZ vs. -30 dBZ) as well as a smaller footprint (0.8 km vs. 1.4 km) and shorter along track integration (500 m vs 1.1 km).

Spaceborne radars operate from platforms that orbit the Earth at speeds that exceed 7 km^{-1}, and employ relatively long pulses to map the vertical structure of hydrometeors in the atmosphere. The strongest echo a spaceborne radar detects is from

the Earth's surface. Instrument simulators are a well-established methodology for accounting for the effects of the observing system sampling geometry on its performance (i.e., detection limit, measurement uncertainty). For example, Lamer et al. (2020) developed an instrument forward simulator to evaluate the impact of different spaceborne CPR configurations on our ability to detect low-level clouds and precipitation using ground-based radar data as an input dataset. Along the same lines Kollias et al. (2022) developed a forward simulator to evaluate the quality of spaceborne Doppler velocity measurements using numerical model output as input dataset. Furthermore, instrument simulators are very useful when comparing observations from different observing systems or when objectively comparing observations and models Lamer et al. (2018).

This study describes Orbital-Radar, an open-source instrument simulator that emulates the EarthCARE and CloudSat CPR instrument capabilities by transforming sub-orbital measurements from various standardized sources and Numerical Weather Prediction (NWP) data into CPR-like observations. Orbital-Radar does not include a forward model that converts microphysical and dynamical variables from a numerical model to radar observables like other existing radar simulators (Oue et al., 2020; Mech et al., 2020). The input is radar parameters from one coordinate system (i.e., profiling cloud radar or numerical model) and the output is CPR synthetic observations. Orbital-Radar employs a combination of functions captured in the flowchart presented in Figure 1. This study demonstrates Orbital-Radar's flexibility and its use to evaluate future applications by testing current EarthCARE CPR configurations by contrasting its results with findings from the literature on the performance of the EarthCARE CPR (Lamer et al., 2020; Kollias et al., 2022).

The study is organized as follows: Section 2 gives an overview of the datasets that can be used as input to Orbital-Radar and discusses the input data sets and their quality control. Section 3 describes the different modules of Orbital-Radar and its limitations. In section 4, example cases are presented to demonstrate Orbital-Radar's performance in scenes with shallow convective clouds, marine stratocumulus clouds, and Arctic clouds. The summary and outlook are provided in Section 5.

2 Input data

The 'orbital-radar' tool transforms ground-based, airborne, or simulated NWP radar data into synthetic satellite data from spaceborne cloud profiling radar (CPR). The quality of the forward simulated CPR data strongly depends on the quality of the input data set; therefore, rigorous quality control is crucial. Furthermore, a harmonized quality assurance allows a better comparison of calculated synthetic CPR data from different sites. 'Orbital-radar' allows several data formats form ground-based radar networks and airborne radars. The paper hadles also forward simulated radar data from Numerical Weather Prediction model output.

- **Ground-based radar data:** Over the last 20 years, the suborbital capabilities for atmospheric research largely increased (Lamer et al., 2023). The U.S. Department of Energy (DoE) Atmospheric Radiation Measurement (ARM) user facility operates several fixed and mobile observatories (Kollias et al., 2020) and the European Union (EU) Aerosol, Clouds, and Trace Gases Research Infrastructure (ACTRIS, Laj et al., 2024) research infrastructure operates over 30 fixed observatories. Furthermore, the number of ground-based observatories, e.g. supersites in Jülich, Germany, (Löhnert et al., 2015), Hyytiälä, Finland, (Hirsikko, 2014), and Barbados (Stevens et al., 2016) extended by mobile observing capabilities, e.g.,

the Leipzig Aerosol and Clouds Remote Observations System (LACROS, Bühl et al., 2013) from the Leipzig Institute for Tropospheric Research, TROPOS. In addition to ground-based sites, several airborne platforms with radar instruments are currently available.

- **Airborne radar data:** Orbital-radar supports data sets from the airborne radars Microwave Radar/radiometer for Arctic Clouds - active (MiRAC-A) onboard *Polar 5* (Mech et al., 2022; Schirmacher et al., 2023) and the Radar Airborne System Tool for Atmosphere (RASTA) onboard *Falcon* (Bouniol et al., 2008; Delanoë et al., 2013).

  If the input data are from an airborne nadir-pointing radar, then the radar signal propagates into the hydrometeor layer in the same direction as that of a spaceborne radar, and no restriction to the type of cloud and precipitation systems is necessary.

- **Numerical Weather Prediction data input:** This is also applicable to input radar data from a numerical model forward modelled to radar observations. In this case, a forward radar operator such as the Passive and Active Microwave radiative TRAnsfer tool (PAMTRA; Mech et al. (2020)) and the Cloud-Resolving Model Radar Simulator (CR-SIM; Oue et al. (2020) is required to convert the model variables to radar parameters. In this case, the forward radar operator can apply the appropriate direction (top-down) two-way 94 GHz attenuation due to hydrometeors and gases. Hereafter, surface and airborne radar and numerical model data are called suborbital data.

Orbital-Radar is capable of ingesting data from several standardized data formats of vertically-pointing radar data including those from the ESAs Generic Earth Observation Metadata Standard (GEOMS), the ACTRIS research infrastructure project, and the DOE ARM user facility (Kollias et al., 2005, 2007). Airborne data sets from MIRAC-A and RASTA are supported.

The optimal use of the tool requires quality-controlled radar data as input (Mech et al., 2022; Schirmacher et al., 2023; Bouniol et al., 2008; Delanoë et al., 2013). If the input radar data are from a 35 GHz radar system, then, the technique described in Protat et al. (2010) is used to convert them to 94 GHz~~and the~~ . The assumption of the transformation relies on an assumption about the mass–diameter relationship of ice particles used in the Mie scattering computations. the disparity in radar reflectivity between 35 GHz and 94 GHz begins to exceed 1 dB when the 35 GHz reflectivity reaches approximately 0 dBZ. In most cases the 35 GHz radar ice reflectivities fall below 0 dBZ. Therefore, any uncertainty arising from this approximation is deemed insignificant (Protat et al., 2010; Kollias et al., 2019). Also the the same dielectric constant (~~$k = 0.75$~~$|k|^2 = 0.75$) is used to estimate radar reflectivity (Ze). This ~~is~~ step is done to match the the satellite configuration. This is mainly used for the ACTRIS data sets and will be applied during the data preparation of orbital radar.

The GEOMS datasets are corrected for gas attenuation using the ACTRIS data product (Tukiainen et al., 2020) which can be selected in the code and will also be applied during the data preperation step of the tool. In contrast, the ARM ARSCL contains a radar dataset already corrected for gas attenuation. The gaseous attenuation is straightforward and requires only knowledge of the vertical profile of water vapour that can be retrieved from an atmospheric sounding (Liebe and Layton, 1987). Knowledge of the hydrometeor phase, mass, density, and number concentration is needed for the estimation of the hydrometeors attenuation. These microphysical parameters are not available from ground-based radar observations. As a result, the surface-up and space-down view of strongly attenuating cloud and precipitation systems is very different and the comparison of these views using

Orbital-Radar is not recommended. Since the tool only has the Ze and Vm fields as input and uses no additional data or retrievals a flagging of cases with high attenuation due to liquid droplets or precipitation is not provided. Such filtering has to be done using additional information, such as Cloudnet target classification or the liquid water path (LWP) by a parallel measuring microwave radiometer. If the input data are from a ground-based radar system, they should be restricted to cases with limited attenuation such as ice clouds and shallow systems. Nevertheless, the filtering of the data depends on the user of the data sets and might be individual and has to be specified when using the data farther.

If the input data are from an airborne nadir-pointing radar, then the radar signal propagates into the hydrometeor layer in the same direction as that of a spaceborne radar, and no restriction to the type of cloud and precipitation systems is necessary.

3 Spaceborne CPR forward simulator

The core components of Orbital-Radar have been separately described in Tanelli et al. (2002); Kollias et al. (2014b); Lamer et al. (2020); Kollias et al. (2022) and used in the code. These are i) the introduction of the Earth's surface radar reflectivity and the response of point target into the range gates above and below the surface (effect of the oversampling of the CPR), ii) the application of the CPR antenna pattern weighting function, iii) the application of the CPR range weighting function considering the details of the transmitter pulse characteristics and the CPR receiver characteristics, iv) the along-track integration, v) the estimation of the Doppler velocity errors, vi) the estimation of the ~~NUBF effects~~ non-uniform beam filling ($NUBF$) effect on the CPR radar reflectivity and Doppler velocity, and vii) the estimation of the CPR signal-to-noise ratio (SNR), which determines the random error in the CPR radar observables along with the along-track integration. The following sections describe the transformations and assumptions in Orbital-Radar. ~~In the following~~ Following the flowchart (figure 1) we describe how they are implemented and treated within the orbital-radar tool.

3.1 Simulation of synthetic CPR data

This section describes the processes depicted in the central dashed box in Figure 1. All technical specifications of the Earth-CARE and Cloudsat CPR mentioned below are listed in Table 1. A table of all variables written in the netCDF output file is presented in the Appendix A, Table A1.

– **Data preparation, coordinate conversion**: Ground-based observations are typically recorded as a function of time and range, i.e., height above ground. Orbital-radar converts time (t) to along-track distance (d) by assuming a constant horizontal wind speed (v_h) throughout the whole atmosphere:

$$d = v_h \cdot t. \tag{1}$$

The range is converted to height above ground by simply adding the surface elevation. Using a mean horizontal wind for the entire depth of the atmosphere that contains the radar observations is often not a good approximation given the variability of the wind magnitude and direction with altitude. At the same time, the profile of the hydrometeor layers

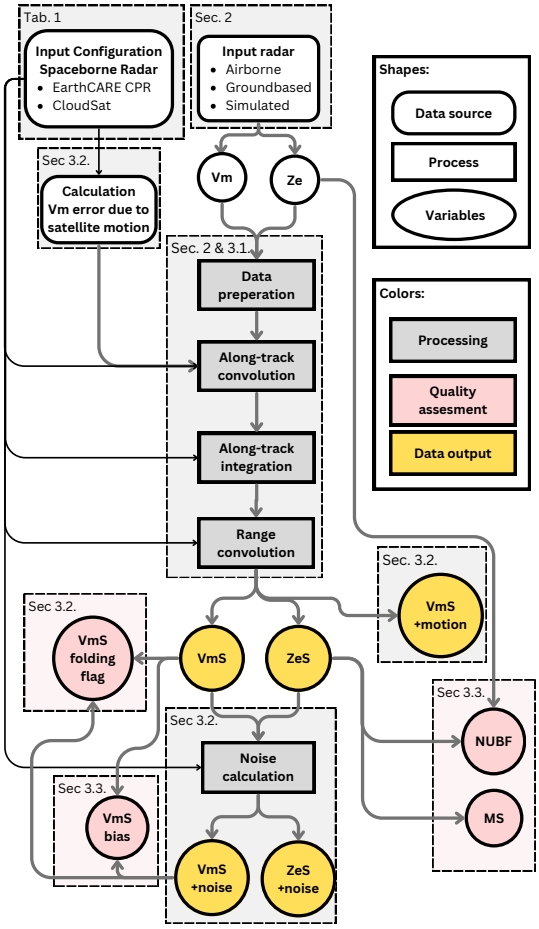

Figure 1. Flowchart of Orbital-Radar. Dashed boxes reference the respective Sections and Tables. The variables are radar reflectivity (Ze), Doppler velocity (Vm), noise-free CPR radar reflectivity (Ze_S), noise-free CPR Doppler velocity (Vm_S), CPR Doppler velocity with satellite motion ($Vm_S + motion$), CPR radar reflectivity with noise ($Ze_S + noise$), Doppler velocity with satellite motion and noise ($Vm_S + noise$), multiple scattering (MS), non-uniform beam filling ($NUBF$), folding flag ($Vm_S\ folding\ flag$), and Doppler velocity bias ($Vm_S\ bias$).

observed by the ground-based radar captures the actual vertical structure of hydrometeors and should be altered. In the case of airborne and model data, the coordinates are already along-track distance and height.

– **Data preparation, introduction of surface echo**: The magnitude and vertical extent of the Earth's surface radar echo determine the "effective" sensitivity of the CPR in the lowest kilometre of the atmosphere (Lamer et al., 2020). The normalized (per unit of area) cross-section of the Earth's surface σ_0 [m^{-1}] represents the magnitude of the Earth's surface echo. Over an ocean surface, the normalized cross section is calculated using the relationship from Li et al. (2005) as a function of the near-surface wind speed provided in the X-MET data product. At 94-GHz, the ocean surface

σ_0 varies between 16 to 6 dB for near-surface wind speeds of 2 to 20 ms^{-1} respectively (Tanelli et al., 2008). At 94-GHz, the ocean σ_0 has negligible dependency on salinity or air temperature. Here, the Li et al. (2005) parameterization is used to model the σ_0 as a function of near-surface for a nadir pointing CPR. Orbital radar is currently optimized for overland is used, therefore the calculation of optimized σ_0 as a function of wind information is not implemented for data sets. Instead, a fixed value is used. Overland, σ_0 exhibits large variability due to its dependency on vegetation, surface slope, soil moisture, snow cover, and other factors (Haynes et al., 2009). Thus, a fixed value of ~~52 dB~~ $\sigma_0 = 52$ dB is used. However, the user can change the value depending on the regional statistics of σ_0 or for overseas scenes. The reflectivity value of the surface echo is simulated by introducing a ground echo into the original measurements. Therefore a Gaussian distribution is added to the measurements with its peak at the range bin below the surface a peak of σ_0 and a width of z_{res}. The correct representation of the surface echo is performed by the along-range convolution. The range weighting function allows us to reproduce the vertical structure of the Earth's surface echo, thus creating the radar blind zone near the surface.

– **Along track convolution (spatial filtering)**: The three-dimensional pattern of the CPR pulse is described by the antenna gain weighting function $W_{ant}(x, y)$ where x and y represent the distance from the line of sight in the cross-radial direction and the range weighting function $W_{range}(r)$ where r is the distance from the center of the CPR pulse along the radial direction (Kollias et al., 2014b; Tanelli et al., 2002) (Donovan et al. (2023) provide an overview of the antenna pattern and the along track weighting functions to represent them in simulation). Cross-track effects are not represented in Orbital-Radar since the ground-based and airborne radar datasets are two-dimensional (time and height). Therefore, Orbital-Radar assumes cross-track homogeneity for all inputs. The ~~$W(x)$~~ $W_x(x)$ for CloudSat is given by:

$$W_x(x) = \exp\{-2 \cdot \ln(2)(\frac{x}{0.5 \cdot IFOV})^2\} \ , \tag{2}$$

where x is the along-track distance between suborbital observation and CPR line of sight, and $IFOV$ is the CPR instantaneous field of view (Table 1).

– **Along range convolution**: The range weighting function $W_r(r)$ depends on the transmitted waveform. The EarthCARE and CloudSat CPRs transmit a 3.3 μs unmodulated pulse and $W_{range}(r)$ is given by:

$$W_r(r) = \exp\{-C_{wr} \cdot \ r^2\} \ , \tag{3}$$

where r is the distance between suborbital observation and CPR pulse centre, and C_{wr} is the range weighting constant (Table 1). However, the transmitted pulse shape and frequency modulation are not the only parameters determining the detailed shape of the $W_{range}(r)$. The EarthCARE CPR uses a receiver filter that generates a sharp cut of the range side-lobes in heights above Earth's surface (Lamer et al., 2020). Therefore, the range weighting function for the EarthCARE CPR is imported from a text file. Lamer et al. (2020) contains a detailed description of the effect of the range weighting function and provided us the range weighting function used in the tool. The $W_r(r)$ and $W_x(x)$ describe the instantaneous spatial filter of the CPR and are used to estimate the CPR reflectivity Ze_{EC} and Doppler velocity V_{EC} using the methodology described in Kollias et al. (2023a); Donovan et al. (2023).

– **Along-track integration**: In addition to the radar spatial filtering, the integration of the radar signal in the along-track introduces a temporal "stretching" filter. The integration of the convoluted data is performed according to the CPR along-track integration length (x_{int}; see Tab. 1).

– **Radar detection**: The minimum detectable signal (MDS) of the CloudSat and EarthCARE CPRs is determined by the CPR receiver noise (N) and the number of integrated radar samples M to estimate a CPR profile. The CPR receiver noise (N) is reported in dBZ units to facilitate the comparison with the radar reflectivity of clouds and precipitation (Table 1). The N values for CloudSat and EarthCARE are -15 and -21.5 dBZ, respectively. Using the N values and the received signal S strength (in dBZ), the Signal-to-Noise ratio (SNR) can be estimated. The SNR is used in the next section to estimate the uncertainty of the CPR measurements. For a $PRF = 7000Hz$ and 500 m along track integration, the EarthCARE CPR uses $M = 486$ samples per estimate, and for a $PRF = 4300Hz$ and 1100 m along track integration, the CloudSat CPR uses $M = 656$ samples per estimate. The integration of M samples suppresses the variance of the CPR receiver noise and allows the detection of weak signals at negative SNR values. The CloudSat MDS is set to -30 dBZ and for EarthCARE is set to -35 dBZ. The MDS values are valuable for estimating which parts of cloud and precipitation systems are detected by the CPRs.

3.2 CPR measurement uncertainty

The uncertainty in the CPR reflectivity is estimated using Hogan et al. (2005) and Delanoë and Hogan (2010).

$$\Delta Z = \frac{4.343}{\sqrt{M}}(1 + \frac{N}{S}) \tag{4}$$

where ΔZ is the standard deviation of the CPR radar reflectivity, M is the number of samples and and $\frac{N}{S}$ is the noise-to-signal ratio in linear units. The CPR reflectivity errors for EarthCARE and CloudSat calculated with Equation 4 are shown in Table 2.

The ΔZ in dB is subsequently used to add noise to the simulated CPR reflectivities:

$$Ze_{+noise} = Ze + \Delta Z_{EC} \cdot \Gamma_{Ze}, \tag{5}$$

where Γ_{Ze} is a Gaussian distributed random number ($\mu = 0, \sigma = 1$, and $\Gamma_{Ze}(x)$ with ~~$x \in [-3, 3]$ (Kollias et al., 2022; Donovan et al., 2023))~~$x \in [-3$ dB$, 3$ dB$]$. In the final step, all data points below the noise floor of CPR N are filtered out from the data.

The satellite velocity V_{sat}, antenna pointing knowledge and the presence of NUBF conditions within the radar sampling volume can lead to biases and uncertainty in the EarthCARE CPR Doppler velocity estimation (Tanelli et al., 2005; Battaglia and Kollias, 2015; Kollias et al., 2022). In Orbital-Radar, the EarthCARE CPR Doppler velocity estimation accounts for the CPR spatial volume filter and along-track integration. Furthermore, every suborbital radar point within the CPR sampling volume has been assigned an apparent Doppler velocity V_x given by:

$$V_x = -x \cdot \frac{V_{sat}}{h_{sat}}, \tag{6}$$

Table 1. Parameters for transforming suborbital radar data to synthetic CPR data (Stephens et al., 2008; Kollias et al., 2014b; Lamer et al., 2020).

Name	Variable	EarthCARE	CloudSat
Frequency	ν	94.05 GHz	94.05 GHz
Satellite velocity	V_{sat}	7200 $\mathrm{km\,s^{-1}}$	7000 $\mathrm{km\,s^{-1}}$
Satellite altitude	h_{sat}	400 km	720 km
Antenna diameter	d_{ant}	2.5 m	1.85 m
Pulse length	r_{pul}	500 m	480 m
Vertical resolution	z_{res}	100 m	240 m
Along-track integration length	x_{int}	500 m	1100 m
Pulse repetition frequency	PRF	~~5000~~6000 Hz	4000 Hz
Noise floor	N	-21.5 dBZ	-15 dBZ
Minimum detectable signal	MDS	-35 dBZ	-30 dBZ
Surface echo equivalent reflectivity	~~Ze_{z_0}~~ σ_0	52 dBZ	52 dBZ
Nyquist velocity	v_{nq}	$\frac{\lambda \cdot PRF}{4}$	-
Antenna beam width	θ_{track}	$\frac{74.5 \cdot \lambda}{d_{ant}}$	$\frac{67 \cdot \lambda}{d_{ant}}$
Range weighting constant	c_{wr}	asymmetric	$\frac{\pi^2}{2 \cdot \ln(2) \cdot r_{pul}^2}$
Instantaneous field of view	$IFOV$	$h_{sat} \cdot \tan\{\frac{\pi \cdot \theta_{track}}{180^\circ}\}$	
Wavelength	λ	$\frac{c}{\nu}$	
Speed of light	c	299792458 $\mathrm{m\,s^{-1}}$	

where V_{sat} is the satellite velocity, h_{sat} is the satellite orbit height and x is the along-track distance of the suborbital radar point from the line of sight. The introduction of V_x permits the estimation of the NUBF-induced velocity bias V_{NUBF} and it is reported in the output file. Using the methodology described in Kollias et al. (2023a), the V_{NUBF} is removed using the along-track CPR reflectivity gradient $\Delta_x Z$. Due to uncertainty in the detail along-track CPR reflectivity structure, the NUBF correction is not perfect and an error term is introduced:

$$std(V_{NUBF}) = 0.15\ \mathrm{m\,s^{-1}} \cdot \frac{\Delta_x Z}{3\ \mathrm{dBZ}} \tag{7}$$

is a result based on statistics from EarthCARE CPR simulations using realistic numerical model scenes and actual cloud observations (Kollias et al., 2022). Equation 7 suggests that the uncertainty in the removal of the V_{NUBF} velocity bias is proportional to the along-track CPR reflectivity gradient $\Delta_x Z$. In typical cloud and precipitation conditions, the median value of $\Delta_x Z$ is approximately 3 $dBkm^{-1}$ (Kollias et al., 2014a), however, in convective clouds can exceed 10 $dBkm^{-1}$. In addition to $std(V_{NUBF})$, the satellite velocity V_{sat} broadens the Doppler velocity distribution (Eq. 6) within the CPR sampling volume, thus, introduces another uncertainty term $std(V_{BROAD})$ (Battaglia et al., 2020a; Kollias et al., 2022, 2014b). The magnitude of $std(V_{BROAD})$ depends on M and SNR. Numerical simulations of time series of radar signals with the same characteristics

Table 2. Parameters for the calculation of Ze and v_m noise as a function of radar reflectivity. ΔZ_{CS} is based on Hogan et al. (2005) and std(V_{TOTAL}) is based on Kollias et al. (2022).

Ze in dB	ΔZ_{CS} in dB	ΔZ_{EC} in dB	std(V_{TOTAL}) in $\mathrm{m\,s^{-1}}$
-37	-	7.18	3.27
-34	-	3.69	3.12
-31	6.92	1.94	2.83
-28	3.55	1.06	2.35
-25	1.85	0.62	1.63
-22	1.01	0.39	1.09
-19	0.58	0.28	0.76
-16	0.36	0.21	0.59
-13	0.24	0.18	0.52
-10	0.18	0.16	0.49
-7	0.14	0.15	0.48
$\geq$-4	0.1	0.13	0.47

like those expected from the EarthCARE CPR have been used to estimate a $std(V_{BROAD})$ lookup table (Table 2). Finally, these two ~~error~~ terms are combined to ~~estimate the total CPR Doppler velocity uncertainty These two terms are combined to~~ provide the total CPR Doppler velocity uncertainty $std(V_{DOP})$:

$$std(V_{DOP}) = \sqrt{std(V_{NUBF})^2 + std(V_{BROAD})^2} \tag{8}$$

Calculation of the synthetic CPR Doppler velocity uncertainty (V_{+noise}) is added on top of the synthetic noise-free CPR with satellite motion contribution data V_{EC} as follows,

$$V_{+noise} = V_{EC} + std(V_{DOP})\,\Gamma_{Vm} \tag{9}$$

where Γ_{Vm} is a Gaussian distribution of random number ($\mu = 0$, $\sigma = 1$, and $\Gamma_{Vm}(x)$ with $x \in [-v_{nq}, v_{nq}]$) representing the general Doppler velocity error statistic of the satellite.

3.3 Quality flags of synthetic CPR data

Orbital-radar produces several diagnostic parameters and flags to help the user assess the quality of the simulated CPR data. The input suborbital data have higher resolution than the CPR simulated data, thus, with the use of the CPR spatial filters we can provide estimates of the NUBF conditions within the CPR sampling volume. The NUBF effects are amplified in areas with significant changes in the microphysics and dynamics and near cloud edges (Pfitzenmaier et al., 2019). The standard deviation of the radar reflectivity field within the CPR sampling filter $std(Ze)$ is used to characterize the representiviness of the simulated

CPR radar reflectivity see Section 4.1, Figure 2 f). In addition, the NUBF Doppler velocity bias V_{NUBF} and the $std(V_{NUBF})$ measure of the impact of NUBF in the CPR Doppler velocity estimate.

The MS flag calculation is based on the method from Battaglia et al. (2008). The ~~flag~~ MS flag using thresholds calculating of MS is present within the column. The thresholds were estimated using Monte Carlo reflectivity simulations for multiple cloud scenes and validated using CloudSat data. EarthCARE also operates at w-band, so we adopted the method, and so the flag highlights all bins in which MS plays a role. The calculation uses an MS scattering threshold of 12 dB or if the integration of the pixels from the top exceeds 42 dB. The flag highlights the profiles affected by MS and provides help for the interpretation of the data.

Finally, the Doppler velocity folding flag identifies CPR data where the simulated Doppler velocity exceeds the Nyquist velocity of the EarthCARE CPR.

4 Application

This section demonstrates the application of Orbital-Radar to four observed or simulated suborbital cloud and precipitation scenes. The first two scenes cover ground-based observations of shallow convective clouds (Sect. 4.1) and marine stratocumulus clouds (Sect. 4.2). The latter two scenes cover airborne observations (Sect. 4.3) and numerical model simulations (Sect. 4.4) of Arctic mixed-phase clouds. Orbital-Radar transforms the suborbital data to EarthCARE CPR observations with the specifications in Table 1. We use a mean horizontal wind of 6 $\mathrm{m\,s^{-1}}$ for ground-based and numerical model input.

4.1 Ground-based: Shallow convective clouds

The first case study presents shallow convective clouds observed by the ground-based 94 GHz radar MiRAC-A at the Jülich Observatory for Cloud Evolution (JOYCE; Löhnert et al., 2015) in Jülich, Germany, on 6 April 2021 (Fig. 2). Snow and graupel were detected and near-surface air temperatures were about 0°C on this day. MiRAC-A observed radar reflectivities above 15 dBZ inside the convective cores and Doppler velocities up to 2 $\mathrm{m\,s^{-1}}$ in updraft regions. We expect attenuation of the radar signal by frozen hydrometeors only due to the absence of a melting layer and the cold near-surface air temperatures.

Figure 2c and Figure 2d illustrate the impact of the EarthCARE CPR sampling volume on the small-scale reflectivity and Doppler velocity features observed by MiRAC-A. These findings are consistent with previous studies (Burns et al., 2016; Lamer et al., 2020). Figure 2e shows the EarthCARE CPR Doppler velocity with NUBF and satellite motion effects, and velocity folding due to the narrow Nyquist velocity. The simulated CPR Doppler velocity illustrates the challenges related to the measurement of convective motions from space (Kollias et al., 2022). For example, although the updrafts detected by the high-resolution ground-based radar are visible in the convoluted and integrated mean Doppler velocity (Figure 2d, the identification of the updraft regions is far more challenging in the Doppler velocity field (Figure 2e. The three diagnostics indicate NUBF near cloud edges and convective cores (Fig. 2f), multiple scattering for the cloud at 270 km (Fig. 2g), and Doppler velocity folding for few scattered range gates near cloud edges (Fig. 2h).

4.2 Ground-based: Marine stratocumulus clouds

The second case study using ground-based radar observations is marine stratocumulus (Figure 3). The measurements were obtained by the 94 GHz National Institute of Research and Development for Optoelectronics (INOE) radar during ASKOS campaign in Mindelo, Cape Verde, on 15 July 2022 (Marinou et al., 2023).

Figure 3a shows the ground-based radar reflectivity of the stratocumulus clouds. The cloud layer is less than 250 m thick and drizzle appears below the cloud base early in the along-track segment. Figure 3b illustrates the vertical stretching of the cloud layer due to the 500 m pulse length of EarthCARE CPR. This pulse length also causes a surface echo up to 500 m above ground (Burns et al., 2016). Figure 3c shows the Doppler velocity from the ground-based radar and Figure 3d the corresponding simulated EarthCARE CPR Doppler velocity. The CPR Doppler velocity field is noisy due to the low SNR and considerable NUBF conditions. Post-processing of the raw CPR Doppler velocities can lead to substantial improvement of their quality (Sy et al., 2014; Kollias et al., 2014b, 2023b).

4.3 Airborne: Arctic mixed-phase clouds

Figure 4 shows the 94 GHz measurements from MiRAC-A on board the *Polar 5* aircraft during the AFLUX campaign near Svalbard, Norway (Mech et al., 2022; Schirmacher et al., 2023). The airborne MiRAC-A does not provide Doppler velocities due to the 25 $^\circ$ off-nadir view of the antenna (Mech et al., 2019). The synthetic $Ze_{EC+noise}$ captures the features of the input radar reflectivity. However, a smoothing effect occurs around the cloud edges. Additionally, the ground echo covers the precipitation near the surface. One should note that the along-track resolution of the input data set is coarser than that of ground-based radars. This generally results in less resolved cloud structures and lower values of the NUBF estimations in the lowest 0.8 km for larger distance 80 km along-track (b) where large gradients in the Ze-fields are visible (a). This case demonstrates the successful transformation of airborne radar data into synthetic CPR data to study satellite overflights (Schirmacher et al., 2023).

4.4 Numerical model: Arctic mixed-phase clouds

The last case presents an Arctic cloud system simulated with a numerical model and converted to radar observation space with the forward operator PAMTRA (Mech et al., 2020). The comparison of these forward simulations with radar observations allows for an evaluation of the simulated microphysical processes in the numerical model (Ori et al., 2020). Figure 5 depicts a forward-simulated scene from the high-resolution icosahedral non-hydrostatic large-eddy model (ICON-LEM; Heinze et al., 2017; Schemann and Ebell, 2020) converted to the EarthCARE CPR data using Orbital-Radar. The ICON data have coarser resolution than surface radar observations, thus, the overall comparison between the modeled and the CPR observations looks very good. Differences are only visible near cloud edges. The smooth reflectivity field also leads to a smaller NUBF contribution; only near cloud edges and regions with high radar reflectivity gradient, the NUBF effects are noticeable. Similarly, the ICON Doppler velocity field is also smooth (Fig. 5c). After conversion to CPR, the Doppler velocity field becomes noisy due to satellite platform motion, which is the largest contributor to the CPR Doppler velocity error (Fig. 5d). In Kollias et al.

(2023a), a procedure to retrieve a smooth best estimate of the hydrometeors sedimentation Doppler velocity in areas with radar reflectivity higher than -15 dBZ is described.

Using forward-modelled numerical model data as input data can have several advantages. First, model data can represent all cloud scenarios. Using tools like PAMTRA or CR-SIM, we first need to convert the model output to radar observables at the resolution of the numerical model. In this case, the CPR hydrometeor attenuation can be directly estimated from the model output using the PAMTRA or CR-SIM forward operators. In the second step, Orbital-Radar is applied to the PAMTRA or CR-SIM output to add the sampling, sensitivity, and uncertainty effects of the spaceborne CPR. This approach can be used to evaluate the performance of future radar systems.

5 Conclusions and outlook

This work describes Orbital-Radar, which transforms suborbital radar measurements into synthetic EarthCARE or CloudSat cloud profiling radar (CPR) data. Orbital-radar used as input standardized sources of ground-based, airborne cloud radar datasets or forward-simulated radar data from numerical models. Input datasets include the European ACTRIS cloud radar network and US DOE ARM observatories. Orbital-Radar reads the different input datasets and, if needed, corrects them for gaseous attenuation and transforms the radar reflectivities from 35 to 94 GHz. In addition, if the input data are from ground-based radar, the time dimension is converted to along track distance by multiplying with a mean wind speed. The quality-controlled input datasets are used to simulate the CPRs by introducing an Earth surface echo, spatial filtering due to the antenna and range weighting functions, and along-track integration. The sensitivity of the spaceborne CPRs is also emulated with the introduction of sensor-specific noise. The introduction of noise affects the detection capability of the CPR and the uncertainty of the key measurements. Noise is then added to the radar moments to reflect how the spaceborne CPR performance is affected by SNR, satellite motion, and NUBF. Finally, Orbital-Radar generates diagnostics to facilitate quality control, i.e., multiple scattering and Doppler velocity folding flags.

The case studies presented demonstrate that Orbital-Radar can reproduce some of the key limitations and challenges introduced by a spaceborne CPR platform. For example, the forward simulations indicate that overall the raw CPR Doppler velocities will be noisy, and careful postprocessing is needed to enhance their quality and application for process understanding and model evaluation. Orbital-Radar facilitates direct comparisons between spaceborne radar observations and surface or airborne radar observations for validation of satellite observations. Furthermore, the tool allows for global high-resolution numerical model evaluation with spaceborne CPR observation when coupling the numerical model output with a radiative transfer model.

Code and data availability. The open-source Orbital-Radar Python package, along with a Jupyter Notebook containing usage examples, is available on Zenodo at (Risse, 2024, https://doi.org/10.5281/zenodo.13375014). The data used in this study can be accessed on Zenodo at (Pfitzenmaier and Risse, 2024, https://doi.org/10.5281/zenodo.12547896). This repository includes PAMTRA simulations of the Ny-

Ålesund ICON-NWP, W-band radar data from JOYCE and Mindelo (in GEOMS format), and airborne MiRAC-A W-band radar data. Ground-based W-band radar data from JOYCE is available on the ACTRIS database (CLU) at (Pfitzenmaier et al., 2024, https://doi.org/10.60656/e8c4957887854659). while ground-based W-band radar data from Mindelo during the ASKOS campaign is accessible on the ACTRIS database (CLU) at (Antonescu et al., 2024, https://doi.org/10.60656/c5e09106ba0246bc). Airborne MiRAC-A W-band radar data collected during the AFLUX campaign is available on the PANGAEA database at (Mech et al., 2022, https://doi.org/10.1594/PANGAEA.965120).

Appendix A

Table A1. List of all variables of the orbital-radar netcdf output file.

output variable	variable description
along_track	along track of the input data
time	time of the input data
range	range of the input data
along_track_sat	along track of the synthetic CPR data
range_sat	range of the synthetic CPR data
sat_ifov	IFOV of the synthetic CPR data
sat_range_resolution	range resolution of the synthetic CPR data
sat_along_track_resolution	along track integration used for the synthetic CPR data
mean_wind	mean horizontal wind used for calculation along track axis transformation
ze	input reflectivity data
vm	input Doppler velocity data
ze_sat	synthetic CPR reflectivity best estimate - noise free
vm_sat	synthetic CPR Doppler velocity best estimate - no satellite motion without noise
vm_sat_vel	synthetic CPR Doppler velocity with satellite motion contribution
ze_sat_noise	synthetic CPR reflectivity with all noise and errors
vm_sat_noise	synthetic CPR Doppler velocity with all noise and errors unfolded
vm_sat_folded	synthetic CPR Doppler velocity with all noise and errors folded
nubf_flag	data flag: Non-uniform beam filling
ms_flag	data flag: Multiple scattering
folding_flag	data flag: Doppler velocity folding

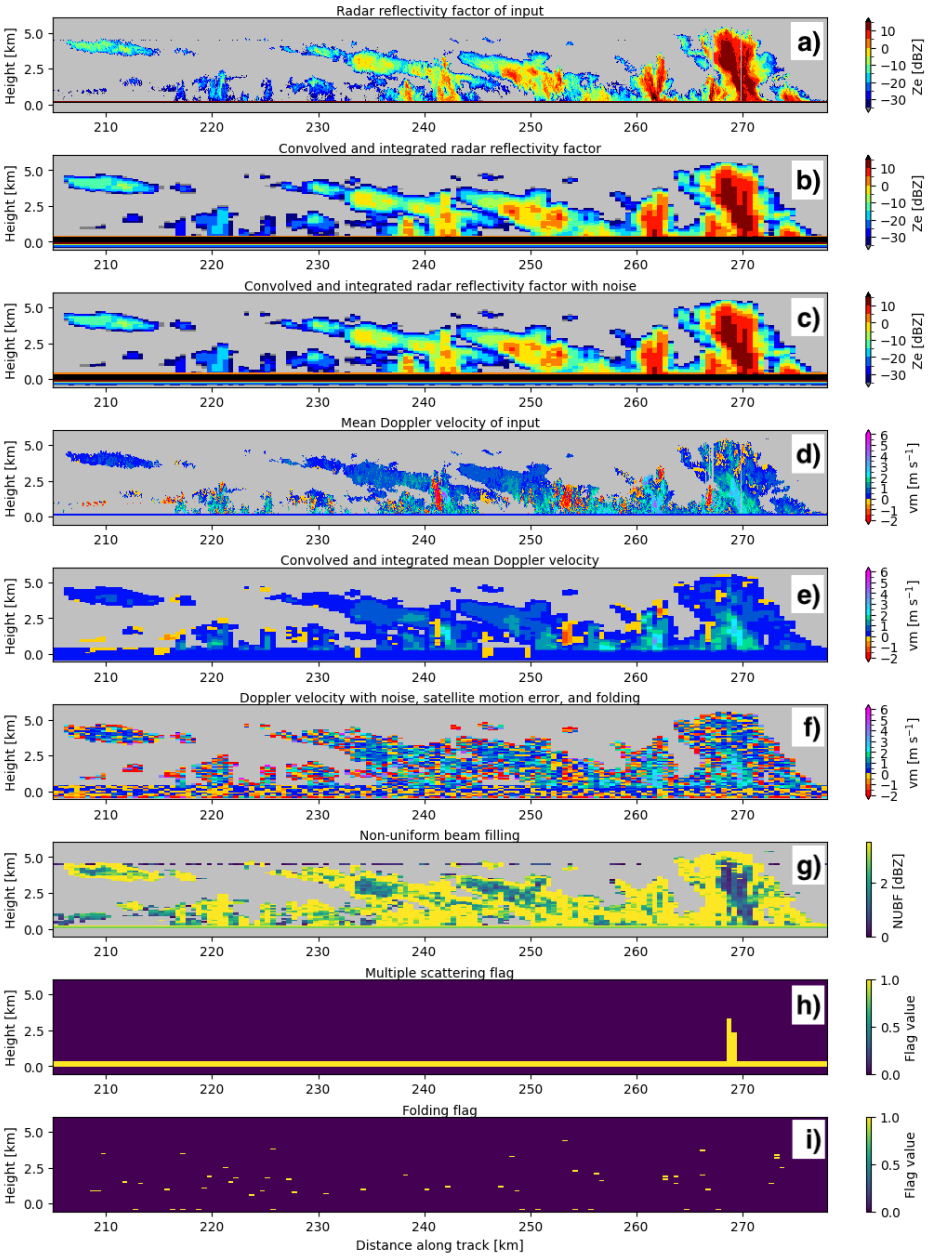

Figure 2. Shallow convective clouds observed by the ground-based MiRAC-A radar at JOYCE in Jülich, Germany, on 6 April 2021 and transformed to EarthCARE CPR with Orbital-Radar. Panels show a zoom of the 24-hour measurements of the (a) input radar reflectivity with artificial surface echo, (b) synthetic CPR radar reflectivity, (c) synthetic CPR radar reflectivity including noise, (~~b~~d) input Doppler velocity, (~~d~~e) synthetic CPR Doppler velocity, (ef) synthetic CPR Doppler velocity including satellite motion, noise, and folding, (fg) NUBF estimate, (~~g~~h) MS flag, and (~~h~~i) folding flag.

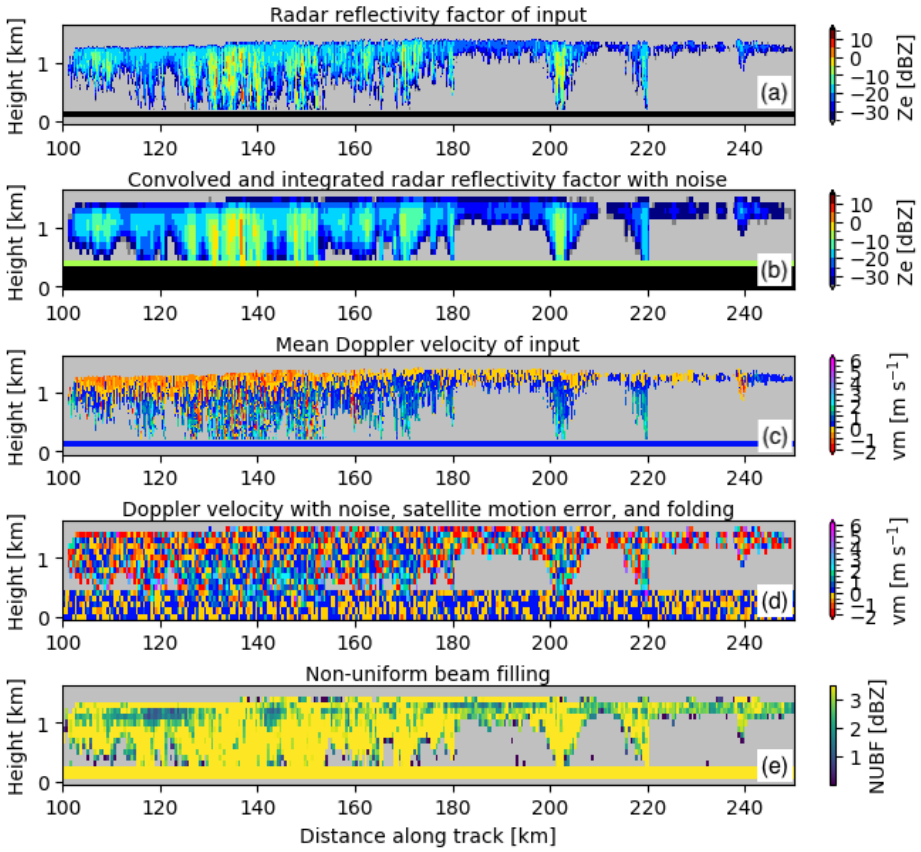

Figure 3. Marine stratocumulus clouds observed by the ground-based INOE radar during ASKOS in Mindelo, Cape Verde, on 15 July 2022 and transformed to EarthCARE CPR with Orbital-Radar. Panels show the (a) input radar reflectivity with artificial surface echo, (b) synthetic CPR radar reflectivity including noise, (c) input Doppler velocity, (d) synthetic CPR Doppler velocity including satellite motion, noise, and folding, and (e) NUBF estimate

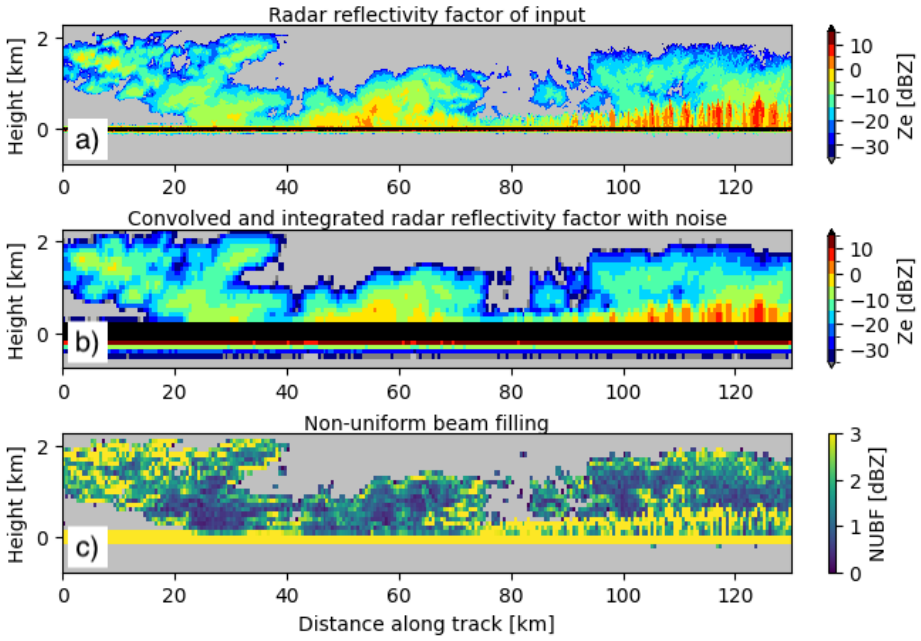

Figure 4. Arctic mixed-phase clouds observed by the airborne MiRAC-A radar onboard *Polar 5* during AFLUX west of Svalbard, Norway, on 1 April 2019 and transformed to EarthCARE CPR with Orbital-Radar. Panels show the (a) input radar reflectivity with artificial surface echo, (b) synthetic CPR radar reflectivity including noise, and (c) NUBF estimate

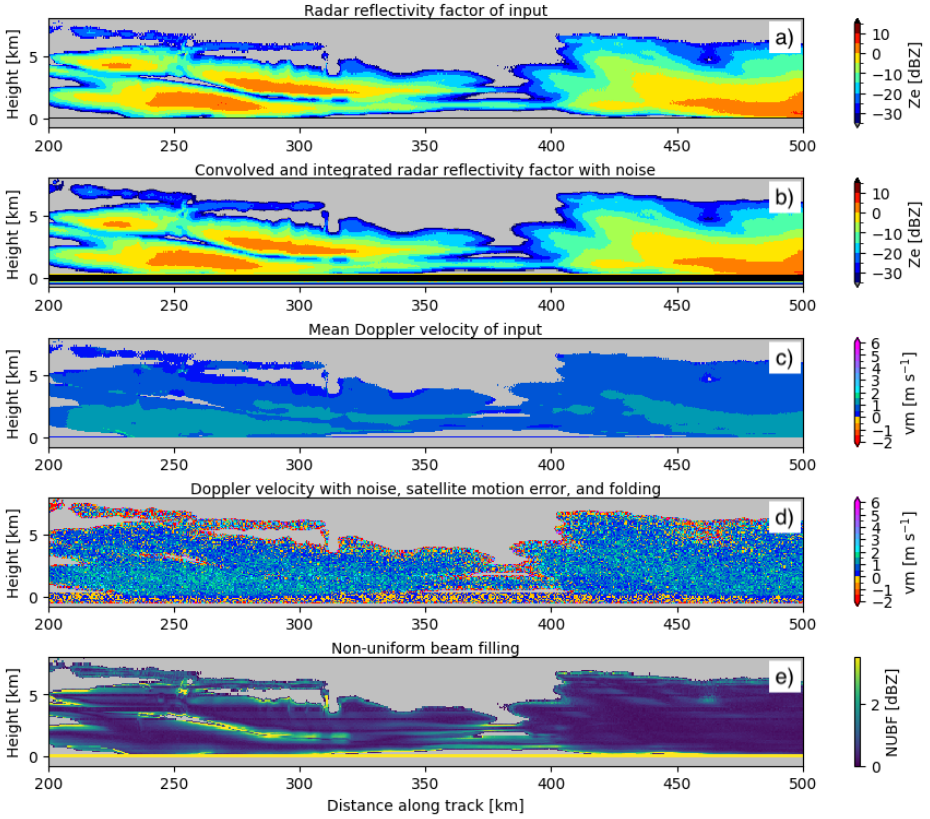

Figure 5. Arctic mixed-phase clouds from the NWP model ICON-LEM forward simulated to a ground-based radar with PAMTRA at AWIPEV in Ny-Ålesund, Svalbard, Norway, on 13 January 2022 and transformed to EarthCARE CPR with Orbital-Radar. Panels show the (a) input radar reflectivity with artificial surface echo, (b) synthetic CPR radar reflectivity including noise, (c) input Doppler velocity, (d) synthetic CPR Doppler velocity including satellite motion, noise, and folding, and (e) NUBF estimate.

Author contributions. LP and PK wrote the original manuscript draft. LP performed the data analysis. NR wrote the Python code based on previous work from LP, IS and KL. PK and BPT helped in the code design and its structure. BPT and KL participated in the review and editing of the manuscript.

Competing interests. The authors declare that they have no conflict of interest.

Acknowledgements. This work was funded, and the code was developed in the scope of ESA-funded projects. The FRM4Radar project (Cloud profiling for Cloud Validation, Contract No. 4000122916/17/I-EF) and ACPV project, Best practice protocol for validation of Aerosol, Cloud, and Precipitation Profiles (Contract No. 4000140645/23/I-NS). Thanks for the support from ESA and the collaboration between the University of Cologne, Stony Brook University, McGill University and Brookhaven National Laboratory. Contributions by KL were supported by the U.S. Department of Energy, Atmospheric System Research (contract: DE-SC0012704).

We acknowledge ACTRIS and Finnish Meteorological Institute for providing the data set which is available for download from https://cloudnet.fmi.fi. We acknowledge ECMWF for providing IFS model data.

References

Antonescu, B., Seifert, P., O'Connor, E., and Fomba, K.: Custom collection of categorize, and model data from Mindelo on 15 Jul 2022, https://doi.org/10.60656/c5e09106ba0246bc, 2024.

Battaglia, A. and Kollias, P.: Using Ice Clouds for Mitigating the EarthCARE Doppler Radar Mispointing, IEEE Transactions on Geoscience and Remote Sensing, 53, 2079–2085, https://doi.org/10.1109/TGRS.2014.2353219, 2015.

Battaglia, A., Haynes, J. M., L'Ecuyer, T., and Simmer, C.: Identifying multiple-scattering-affected profiles in CloudSat observations over the oceans, Journal of Geophysical Research: Atmospheres, 113, https://doi.org/https://doi.org/10.1029/2008JD009960, _eprint: https://agupubs.onlinelibrary.wiley.com/doi/pdf/10.1029/2008JD009960, 2008.

Battaglia, A., Kollias, P., Dhillon, R., Lamer, K., Khairoutdinov, M., and Watters, D.: Mind the gap – Part 2: Improving quantitative estimates of cloud and rain water path in oceanic warm rain using spaceborne radars, Atmospheric Measurement Techniques, 13, 4865–4883, https://doi.org/10.5194/amt-13-4865-2020, 2020a.

Battaglia, A., Kollias, P., Dhillon, R., Roy, R., Tanelli, S., Lamer, K., Grecu, M., Lebsock, M., Watters, D., Mroz, K., Heymsfield, G., Li, L., and Furukawa, K.: Spaceborne Cloud and Precipitation Radars: Status, Challenges, and Ways Forward, Reviews of Geophysics, 58, e2019RG000 686, https://doi.org/https://doi.org/10.1029/2019RG000686, _eprint: https://agupubs.onlinelibrary.wiley.com/doi/pdf/10.1029/2019RG000686, 2020b.

Bouniol, D., Protat, A., Plana-Fattori, A., Giraud, M., Vinson, J.-P., and Grand, N.: Comparison of Airborne and Spaceborne 95-GHz Radar Reflectivities and Evaluation of Multiple Scattering Effects in Spaceborne Measurements, Journal of Atmospheric and Oceanic Technology, 25, 1983 – 1995, https://doi.org/10.1175/2008JTECHA1011.1, place: Boston MA, USA Publisher: American Meteorological Society, 2008.

Bühl, J., Seifert, P., Wandinger, U., Baars, H., Kanitz, T., Schmidt, J., Myagkov, A., Engelmann, R., Skupin, A., Heese, B., et al.: LACROS: the Leipzig aerosol and cloud remote observations system, in: Remote sensing of clouds and the atmosphere XVIII; and optics in atmospheric propagation and adaptive systems XVI, vol. 8890, p. 889002, SPIE, 2013.

Burns, D., Kollias, P., Tatarevic, A., Battaglia, A., and Tanelli, S.: The performance of the EarthCARE Cloud Profiling Radar in marine stratiform clouds, Journal of Geophysical Research: Atmospheres, 121, 525–14, https://doi.org/10.1002/2016JD025090, 2016.

Delanoë, J. and Hogan, R. J.: Combined CloudSat-CALIPSO-MODIS retrievals of the properties of ice clouds, Journal of Geophysical Research: Atmospheres, 115, https://doi.org/https://doi.org/10.1029/2009JD012346, 2010.

Delanoë, J., Protat, A., Jourdan, O., Pelon, J., Papazzoni, M., Dupuy, R., Gayet, J.-F., and Jouan, C.: Comparison of Airborne In Situ, Airborne Radar–Lidar, and Spaceborne Radar–Lidar Retrievals of Polar Ice Cloud Properties Sampled during the POLARCAT Campaign, Journal of Atmospheric and Oceanic Technology, 30, 57 – 73, https://doi.org/10.1175/JTECH-D-11-00200.1, place: Boston MA, USA Publisher: American Meteorological Society, 2013.

Donovan, D. P., Kollias, P., Velázquez Blázquez, A., and van Zadelhoff, G.-J.: The generation of EarthCARE L1 test data sets using atmospheric model data sets, Atmospheric Measurement Techniques, 16, 5327–5356, https://doi.org/10.5194/amt-16-5327-2023, 2023.

Haynes, J. M., L'Ecuyer, T. S., Stephens, G. L., and Jakob, C.: Cloud and precipitation regimes revealed by combined CloudSat and ISCCP observations, AGU Fall Meeting Abstracts, 44, 04, http://adsabs.harvard.edu/abs/2009AGUFM.A44B..04H, 2009.

Heinze, R., Dipankar, A., Henken, C. C., Moseley, C., Sourdeval, O., Trömel, S., Xie, X., Adamidis, P., Ament, F., Baars, H., Barthlott, C., Behrendt, A., Blahak, U., Bley, S., Brdar, S., Brueck, M., Crewell, S., Deneke, H., Di Girolamo, P., Evaristo, R., Fischer, J., Frank, C., Friederichs, P., Göcke, T., Gorges, K., Hande, L., Hanke, M., Hansen, A., Hege, H.-C., Hoose, C., Jahns, T., Kalthoff,

N., Klocke, D., Kneifel, S., Knippertz, P., Kuhn, A., van Laar, T., Macke, A., Maurer, V., Mayer, B., Meyer, C. I., Muppa, S. K., Neggers, R. A. J., Orlandi, E., Pantillon, F., Pospichal, B., Röber, N., Scheck, L., Seifert, A., Seifert, P., Senf, F., Siligam, P., Simmer, C., Steinke, S., Stevens, B., Wapler, K., Weniger, M., Wulfmeyer, V., Zängl, G., Zhang, D., and Quaas, J.: Large-eddy simulations over Germany using ICON: a comprehensive evaluation, Quarterly Journal of the Royal Meteorological Society, 143, 69–100, https://doi.org/https://doi.org/10.1002/qj.2947, _eprint: https://rmets.onlinelibrary.wiley.com/doi/pdf/10.1002/qj.2947, 2017.

Hirsikko, A., e. a.: Observing wind, aerosol particles, cloud and precipitation: Finland's new ground-based remote-sensing network, AMT, 7, 1351–1375, 2014.

Hogan, R. J., Gaussiat, N., and Illingworth, A. J.: Stratocumulus Liquid Water Content from Dual-Wavelength Radar, Journal of Atmospheric and Oceanic Technology, 22, 1207 – 1218, https://doi.org/https://doi.org/10.1175/JTECH1768.1, 2005.

Illingworth, A. J., Barker, H. W., Beljaars, A., Ceccaldi, M., Chepfer, H., Clerbaux, N., Cole, J., Delanoë, J., Domenech, C., Donovan, D. P., Fukuda, S., Hirakata, M., Hogan, R. J., Huenerbein, A., Kollias, P., Kubota, T., Nakajima, T., Nakajima, T. Y., Nishizawa, T., Ohno, Y., Okamoto, H., Oki, R., Sato, K., Satoh, M., Shephard, M. W., Velázquez-Blázquez, A., Wandinger, U., Wehr, T., and Zadelhoff, G.-J. v.: The EarthCARE Satellite: The Next Step Forward in Global Measurements of Clouds, Aerosols, Precipitation, and Radiation, Bulletin of the American Meteorological Society, 96, 1311 – 1332, https://doi.org/https://doi.org/10.1175/BAMS-D-12-00227.1, 2015.

Kollias, P., Albrecht, B. A., Clothiaux, E. E., Miller, M. A., Johnson, K. L., and Moran, K. P.: The Atmospheric Radiation Measurement Program Cloud Profiling Radars: An Evaluation of Signal Processing and Sampling Strategies, Journal of Atmospheric and Oceanic Technology, 22, 930 – 948, https://doi.org/10.1175/JTECH1749.1, place: Boston MA, USA Publisher: American Meteorological Society, 2005.

Kollias, P., Clothiaux, E. E., Miller, M. A., Albrecht, B. A., Stephens, G. L., and Ackerman, T. P.: Millimeter-Wavelength Radars: New Frontier in Atmospheric Cloud and Precipitation Research, Bulletin of the American Meteorological Society, 88, 1608 – 1624, https://doi.org/10.1175/BAMS-88-10-1608, place: Boston MA, USA Publisher: American Meteorological Society, 2007.

Kollias, P., Tanelli, S., Battaglia, A., and Tatarevic, A.: Evaluation of EarthCARE Cloud Profiling Radar Doppler Velocity Measurements in Particle Sedimentation Regimes, Journal of Atmospheric and Oceanic Technology, 31, 366–386, https://doi.org/10.1175/JTECH-D-11-00202.1, 2014a.

Kollias, P., Tanelli, S., Battaglia, A., and Tatarevic, A.: Evaluation of EarthCARE Cloud Profiling Radar Doppler Velocity Measurements in Particle Sedimentation Regimes, Journal of Atmospheric and Oceanic Technology, 31, 366 – 386, https://doi.org/https://doi.org/10.1175/JTECH-D-11-00202.1, 2014b.

Kollias, P., Puigdomènech Treserras, B., and Protat, A.: Calibration of the 2007–2017 record of Atmospheric Radiation Measurements cloud radar observations using CloudSat, Atmospheric Measurement Techniques, 12, 4949–4964, https://doi.org/10.5194/amt-12-4949-2019, 2019.

Kollias, P., Bharadwaj, N., Clothiaux, E. E., Lamer, K., Oue, M., Hardin, J., Isom, B., Lindenmaier, I., Matthews, A., Luke, E. P., Giangrande, S. E., Johnson, K., Collis, S., Comstock, J., and Mather, J. H.: The ARM Radar Network: At the Leading Edge of Cloud and Precipitation Observations, Bulletin of the American Meteorological Society, 101, E588 – E607, https://doi.org/https://doi.org/10.1175/BAMS-D-18-0288.1, 2020.

Kollias, P., Battaglia, A., Lamer, K., Treserras, B. P., and Braun, S. A.: Mind the Gap - Part 3: Doppler Velocity Measurements From Space, Frontiers in Remote Sensing, 3, https://doi.org/10.3389/frsen.2022.860284, 2022.

Kollias, P., Puidgomènech Treserras, B., Battaglia, A., Borque, P. C., and Tatarevic, A.: Processing reflectivity and Doppler velocity from EarthCARE's cloud-profiling radar: the C-FMR, C-CD and C-APC products, Atmospheric Measurement Techniques, 16, 1901–1914, https://doi.org/10.5194/amt-16-1901-2023, 2023a.

Kollias, P., Puidgomènech Treserras, B., Battaglia, A., Borque, P. C., and Tatarevic, A.: Processing reflectivity and Doppler velocity from EarthCARE's cloud-profiling radar: the C-FMR, C-CD and C-APC products, Atmospheric Measurement Techniques, 16, 1901–1914, https://doi.org/10.5194/amt-16-1901-2023, 2023b.

Laj, P., Myhre, C. L., Riffault, V., Amiridis, V., Fuchs, H., Eleftheriadis, K., Petäjä, T., Salameh, T., Kivekäs, N., Juurola, E., Saponaro, G., Philippin, S., Cornacchia, C., Arboledas, L. A., Baars, H., Claude, A., Mazière, M. D., Dils, B., Dufresne, M., Evangeliou, N., Favez, O., Fiebig, M., Haeffelin, M., Herrmann, H., Höhler, K., Illmann, N., Kreuter, A., Ludewig, E., Marinou, E., Möhler, O., Mona, L., Murberg, L. E., Nicolae, D., Novelli, A., O'Connor, E., Ohneiser, K., Altieri, R. M. P., Picquet-Varrault, B., Pinxteren, D. v., Pospichal, B., Putaud, J.-P., Reimann, S., Siomos, N., Stachlewska, I., Tillmann, R., Voudouri, K. A., Wandinger, U., Wiedensohler, A., Apituley, A., Comerón, A., Gysel-Beer, M., Mihalopoulos, N., Nikolova, N., Pietruczuk, A., Sauvage, S., Sciare, J., Skov, H., Svendby, T., Swietlicki, E., Tonev, D., Vaughan, G., Zdimal, V., Baltensperger, U., Doussin, J.-F., Kulmala, M., Pappalardo, G., Sundet, S. S., and Vana, M.: Aerosol, Clouds and Trace Gases Research Infrastructure – ACTRIS, the European research infrastructure supporting atmospheric science, Bulletin of the American Meteorological Society, https://doi.org/10.1175/BAMS-D-23-0064.1, place: Boston MA, USA Publisher: American Meteorological Society, 2024.

Lamer, K., Fridlind, A. M., Ackerman, A. S., Kollias, P., Clothiaux, E. E., and Kelley, M.: $(GO)^2$-SIM: a GCM-oriented ground-observation forward-simulator framework for objective evaluation of cloud and precipitation phase, Geoscientific Model Development, 11, 4195–4214, https://doi.org/10.5194/gmd-11-4195-2018, 2018.

Lamer, K., Kollias, P., Battaglia, A., and Preval, S.: Mind the gap – Part 1: Accurately locating warm marine boundary layer clouds and precipitation using spaceborne radars, Atmospheric Measurement Techniques, 13, 2363–2379, https://doi.org/10.5194/amt-13-2363-2020, 2020.

Lamer, K., Kollias, P., Amiridis, V., Marinou, E., Loehnert, U., Schnitt, S., and McComiskey, A.: Ground-Based Remote-Sensing of Key Properties, pp. 327–360, https://doi.org/https://doi.org/10.1002/9781119529019.ch14, 2023.

Li, L., Heymsfield, G. M., Tian, L., and Racette, P. E.: Measurements of Ocean Surface Backscattering Using an Airborne 94-GHz Cloud Radar—Implication for Calibration of Airborne and Spaceborne W-Band Radars, Journal of Atmospheric and Oceanic Technology, 22, 1033 – 1045, https://doi.org/10.1175/JTECH1722.1, 2005.

Liebe, H. and Layton, D.: Millimeter-wave properties of the atmosphere: Laboratory studies and propagation modeling, http://www.its.bldrdoc.gov/publications/download/87-224.pdf, 1987.

Löhnert, U., Schween, J. H., Acquistapace, C., Ebell, K., Maahn, M., Barrera-Verdejo, M., Hirsikko, A., Bohn, B., Knaps, A., O'Connor, E., Simmer, C., Wahner, A., and Crewell, S.: JOYCE: Jülich Observatory for Cloud Evolution, Bulletin of the American Meteorological Society, 96, 1157 – 1174, https://doi.org/10.1175/BAMS-D-14-00105.1, place: Boston MA, USA Publisher: American Meteorological Society, 2015.

Marinou, E., Paschou, P., Tsikoudi, I., Tsekeri, A., Daskalopoulou, V., Kouklaki, D., Siomos, N., Spanakis-Misirlis, V., Voudouri, K. A., Georgiou, T., Drakaki, E., Kampouri, A., Papachristopoulou, K., Mavropoulou, I., Mallios, S., Proestakis, E., Gkikas, A., Koutsoupi, I., Raptis, I. P., Kazadzis, S., Baars, H., Floutsi, A., Pirloaga, R., Nemuc, A., Marenco, F., Kezoudi, M., Papetta, A., Močnik, G., Díez, J. Y., Ryder, C. L., Ratcliffe, N., Kandler, K., Sudharaj, A., and Amiridis, V.: An Overview of the ASKOS Campaign in Cabo Verde, Environmental Sciences Proceedings, 26, https://doi.org/10.3390/environsciproc2023026200, 2023.

Mech, M., Kliesch, L.-L., Anhäuser, A., Rose, T., Kollias, P., and Crewell, S.: Microwave Radar/radiometer for Arctic Clouds (MiRAC): first insights from the ACLOUD campaign, Atmospheric Measurement Techniques, 12, 5019–5037, https://doi.org/10.5194/amt-12-5019-2019, 2019.

Mech, M., Maahn, M., Kneifel, S., Ori, D., Orlandi, E., Kollias, P., Schemann, V., and Crewell, S.: PAMTRA 1.0: the Passive and Active Microwave radiative TRAnsfer tool for simulating radiometer and radar \textbackslashhack\textbackslashbreakmeasurements of the cloudy atmosphere, Geoscientific Model Development, 13, 4229–4251, https://doi.org/10.5194/gmd-13-4229-2020, 2020.

Mech, M., Ehrlich, A., Herber, A., Lüpkes, C., Wendisch, M., Becker, S., Boose, Y., Chechin, D., Crewell, S., Dupuy, R., Gourbeyre, C., Hartmann, J., Jäkel, E., Jourdan, O., Kliesch, L.-L., Klingebiel, M., Kulla, B. S., Mioche, G., Moser, M., Risse, N., Ruiz-Donoso, E., Schäfer, M., Stapf, J., and Voigt, C.: MOSAiC-ACA and AFLUX - Arctic airborne campaigns characterizing the exit area of MOSAiC, Scientific Data, 9, 790, https://doi.org/10.1038/s41597-022-01900-7, 2022.

Mech, M., Risse, N., Crewell, S., and Kliesch, L.-L.: Radar reflectivities at 94 GHz and microwave brightness temperature measurements at 89 GHz during the AFLUX Arctic airborne campaign in spring 2019 out of Svalbard, https://doi.org/10.1594/PANGAEA.944506, 2022.

Ori, D., Schemann, V., Karrer, M., Dias Neto, J., von Terzi, L., Seifert, A., and Kneifel, S.: Evaluation of ice particle growth in ICON using statistics of multi-frequency Doppler cloud radar observations, Quarterly Journal of the Royal Meteorological Society, 146, 3830–3849, https://doi.org/https://doi.org/10.1002/qj.3875, _eprint: https://rmets.onlinelibrary.wiley.com/doi/pdf/10.1002/qj.3875, 2020.

Oue, M., Tatarevic, A., Kollias, P., Wang, D., Yu, K., and Vogelmann, A. M.: The Cloud-resolving model Radar SIMulator (CR-SIM) Version 3.3: description and applications of a virtual observatory, GMD, 13, 1975–1998, 2020.

Pfitzenmaier, L. and Risse, N.: Orbital-radar.py test data repositroy, https://doi.org/10.5281/zenodo.12547896, 2024.

Pfitzenmaier, L., Battaglia, A., and Kollias, P.: The Impact of the Radar-Sampling Volume on Multiwavelength Spaceborne Radar Measurements Using Airborne Radar Observations, Remote Sensing, 11, https://doi.org/10.3390/rs11192263, 2019.

Pfitzenmaier, L., Pospichal, B., Schween, J., O'Connor, E., and Löhnert, U.: Custom collection of categorize, and model data from Jülich on 6 Apr 2021, https://doi.org/10.60656/e8c4957887854659, 2024.

Protat, A., Delanoë, J., O'Connor, E. J., and L'Ecuyer, T. S.: The Evaluation of CloudSat and CALIPSO Ice Microphysical Products Using Ground-Based Cloud Radar and Lidar Observations, Journal of Atmospheric and Oceanic Technology, 27, 793 – 810, https://doi.org/https://doi.org/10.1175/2009JTECHA1397.1, 2010.

Rapp, A. D., Lebsock, M., and L'Ecuyer, T.: Low cloud precipitation climatology in the southeastern Pacific marine stratocumulus region using CloudSat, Environmental Research Letters, 8, 014 027, https://doi.org/10.1088/1748-9326/8/1/014027, publisher: IOP Publishing, 2013.

Risse, N.: igmk/orbital-radar: orbital-radar_v1.0.0, https://doi.org/10.5281/zenodo.13375014, 2024.

Schemann, V. and Ebell, K.: Simulation of mixed-phase clouds with the ICON large-eddy model in the complex Arctic environment around Ny-Ålesund, Atmospheric Chemistry and Physics, 20, 475–485, https://doi.org/10.5194/acp-20-475-2020, 2020.

Schirmacher, I., Kollias, P., Lamer, K., Mech, M., Pfitzenmaier, L., Wendisch, M., and Crewell, S.: Assessing Arctic low-level clouds and precipitation from above – a radar perspective, Atmospheric Measurement Techniques, 16, 4081–4100, https://doi.org/10.5194/amt-16-4081-2023, 2023.

Stephens, G., Winker, D., Pelon, J., Trepte, C., Vane, D., Yuhas, C., L'Ecuyer, T., and Lebsock, M.: CloudSat and CALIPSO within the A-Train: Ten Years of Actively Observing the Earth System, Bulletin of the American Meteorological Society, 99, 569 – 581, https://doi.org/10.1175/BAMS-D-16-0324.1, place: Boston MA, USA Publisher: American Meteorological Society, 2018.

Stephens, G. L., Vane, D. G., Tanelli, S., Im, E., Durden, S., Rokey, M., Reinke, D., Partain, P., Mace, G. G., Austin, R., L'Ecuyer, T., Haynes, J., Lebsock, M., Suzuki, K., Waliser, D., Wu, D., Kay, J., Gettelman, A., Wang, Z., and Marchand, R.: CloudSat mission: Performance and early science after the first year of operation, Journal of Geophysical Research: Atmospheres, 113, https://doi.org/https://doi.org/10.1029/2008JD009982, 2008.

Stevens, B., Farrell, D., Hirsch, L., Jansen, F., Nuijens, L., Serikov, I., Brügmann, B., Forde, M., Linne, H., Lonitz, K., and Prospero, J. M.: The Barbados Cloud Observatory: Anchoring Investigations of Clouds and Circulation on the Edge of the ITCZ, Bulletin of the American Meteorological Society, 97, 787 – 801, https://doi.org/10.1175/BAMS-D-14-00247.1, 2016.

Sy, O. O., Tanelli, S., Takahashi, N., Ohno, Y., Horie, H., and Kollias, P.: Simulation of EarthCARE Spaceborne Doppler Radar Products Using Ground-Based and Airborne Data: Effects of Aliasing and Nonuniform Beam-Filling, IEEE Transactions on Geoscience and Remote Sensing, 52, 1463–1479, https://doi.org/10.1109/TGRS.2013.2251639, 2014.

Tanelli, S., Im, E., Durden, S. L., Facheris, L., and Giuli, D.: The Effects of Nonuniform Beam Filling on Vertical Rainfall Velocity Measurements with a Spaceborne Doppler Radar, Journal of Atmospheric and Oceanic Technology, 19, 1019 – 1034, https://doi.org/https://doi.org/10.1175/1520-0426(2002)019<1019:TEONBF>2.0.CO;2, 2002.

Tanelli, S., Im, E., Kobayashi, S., Mascelloni, R., and Facheris, L.: Spaceborne Doppler Radar Measurements of Rainfall: Correction of Errors Induced by Pointing Uncertainties, Journal of Atmospheric and Oceanic Technology, 22, 1676 – 1690, https://doi.org/https://doi.org/10.1175/JTECH1797.1, 2005.

Tanelli, S., Durden, S. L., Im, E., Pak, K. S., Reinke, D. G., Partain, P., Haynes, J. M., and Marchand, R. T.: CloudSat's cloud profiling radar after two years in orbit: performance, calibration, and processing, IEEE Transactions on Geoscience and Remote Sensing, 46, 3560–3573, https://doi.org/10.1109/TGRS.2008.2002030, 2008.

Tukiainen, S., O'Connor, E., and Korpinen, A.: CloudnetPy: A Python package for processing cloud remote sensing data, Journal of Open Source Software, 5, 2123, https://doi.org/10.21105/joss.02123, 2020.

Wehr, T., Kubota, T., Tzeremes, G., Wallace, K., Nakatsuka, H., Ohno, Y., Koopman, R., Rusli, S., Kikuchi, M., Eisinger, M., Tanaka, T., Taga, M., Deghaye, P., Tomita, E., and Bernaerts, D.: The EarthCARE mission – science and system overview, Atmospheric Measurement Techniques, 16, 3581–3608, https://doi.org/10.5194/amt-16-3581-2023, 2023.